ACS OMEGA

Open Access

http://pubs.acs.org/journal/acsodf

Article

Population Mass Balance Model for Precipitation with Turbidity Measurements

Paszkál Papp, Ágota Tóth, and Dezső Horváth*

Cite This: *ACS Omega* 2024, 9, 13412−13417

Read Online

ACCESS | Metrics & More | Article Recommendations

ABSTRACT: The discretized population balance theory has been proven to be a useful method to simulate systems in which solid particles are present. In this work, we introduce a new approach to model precipitation reactions based on the temporal evolution of product concentration, from which particle size distribution, its dynamics, and the specific interfacial energies can be obtained. For a reference study, the previously investigated calcium oxalate precipitation was selected, where the reaction was followed via turbidity measurement. From the obtained particle size distribution, we can show that at low supersaturation, growth is the dominant process, while at higher supersaturation, nucleation is the dominant process. Moreover, the temporal change of the distribution curve has allowed us to split the precipitation into a nucleation, a growth-driven intermediate, and a saturation regime. Furthermore, the comparison between the experimental and calculated results has proved that the method is suitable for predicting particle size distributions and specific interfacial energies.

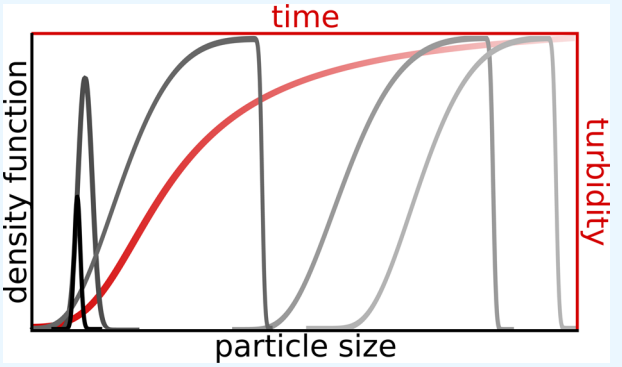

INTRODUCTION

The computational modeling of heterogeneous systems, in which solid or liquid particles are dispersed in a fluid medium, can be a challenging task, therefore it has been in the focus of extensive scientific investigation lately.[1−3] Precipitation can generate such systems; their simulation is especially difficult because the number and sizes of the elements are not stationary. There are processes that increase or decrease the number of particles, such as nucleation, redissolution, or agglomeration, to name a few. Moreover, their sizes can also change dynamically via growth or breakage.[4] Because the system is heterogeneous, it cannot be described by using solely the classical state variables, since the characteristic properties of the dispersed elements, such as their size, habit, structure, or configuration in continuous phase, have to be taken into account as well.[5] In order to simulate systems coupled with precipitation reactions, the size, the composition, and the trajectory of each particle at every time instance must be calculated.[6,7] However, in some cases, for example, in industrial crystallization processes, the number of particles becomes vast to follow them individually.[8] For these cases, the discretized population balance (DPB) model was developed by Hulburt and Katz.[9] In their work, instead of treating particles separately, a density function is used to describe the particle size distribution (PSD) and the evolution of the precipitate. Their formula has been applied in various fields of research, for example, in the modeling of bacteria division,[10] in electrochemistry,[11] or in polymer chemistry.[12]

In many studies concerning DPB modeling, the measured PSD is used to fit the parameters appearing in the density function.[13,14] In this work, we present a method to predict PSDs using temporal precipitate concentration curves. The evolution of product concentration in the case of precipitation can be followed with various experimental techniques, for example, by measuring conductance,[15] dynamic light scattering,[16] or turbidity. The latter can be conveniently monitored utilizing a photometer[17−20] or a high-speed camera.[21] As a case study, a previously investigated calcium oxalate formation[15] is selected, from which the temporal evolution of turbidity for various initial reactant concentrations and the scanning electron microscopy (SEM) images of the products are available. By utilizing our new method, we can predict the PSD to provide information on the precipitate size domain.

MODELING

Governing Equations. Isothermal crystallization is considered where the formation of solid phase is separated into two subprocesses: nucleation, which depends solely on

Received: December 30, 2023
Revised: February 15, 2024
Accepted: February 23, 2024
Published: March 5, 2024

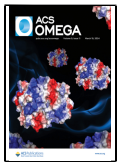

supersaturation S, and particle growth, which is also affected by the surface area of the particles (A_p) according to

$$\frac{\partial n_p}{\partial t} = (r_n(S) + r_g(S, A_p))V \tag{1}$$

where n_p is the amount of substance of the product, V is the volume of the solution, and r_n and r_g are the rates of nucleation and growth, respectively. Due to the large number of particles, their sizes cannot be treated individually; therefore, DPB theory has been applied. The PSD function $f(L)$ is defined as

$$N_p = \int f(L)\mathrm{d}L \tag{2}$$

which is an unnormalized density function, where N_p is the number of particles in the system and L is the particle size. In this model the particles are chosen to be spherical; thus, L is equal to the diameter of the sphere. By taking into account the definition of the PSD function eq 2 and the assumption that the particles are spherical, the total surface area (A_p) and volume (V_p) of the solid phase can be given as

$$A_p = \pi \int L^2 f(L)\mathrm{d}L \tag{3}$$

$$V_p = \frac{\pi}{6} \int L^3 f(L)\mathrm{d}L \tag{4}$$

Since the PSD function is used to describe the number and size distribution of the solid particles, its temporal evolution depends on the formation of the solid phase; therefore, it can also be divided into two subprocesses. Thus, the temporal change of the PSD function can be expressed as

$$\frac{\partial f}{\partial t} = \frac{\partial N_p}{\partial t} g(L) + \left.\frac{\partial f}{\partial t}\right|_{N_p} \tag{5}$$

where the first term corresponds to the nucleation and the second to the growth, and $g(L)$ is a normal distribution function. In our model, solely homogeneous nucleation is considered; hence, the temporal change of the particles is proportional to the rate of nucleation, i.e.,

$$\frac{\partial N_p}{\partial t} \propto r_n \tag{6}$$

We assume that particles do not form with a uniform size, instead, nucleation leads to a certain size distribution[22] $g(L)$, which we approximate with a normal distribution function

$$g(L) = \frac{1}{\sigma\sqrt{2\pi}} \exp\left(\frac{-(L-\mu)^2}{2\sigma^2}\right) \tag{7}$$

where μ and σ is the mean size and its standard deviation, respectively. The mean is set to be $\mu = 1$ μm, matching the upper limit of the colloidal size range.[23] In order to introduce stochasticity into the model, the initial distribution function has to be sufficiently wide; therefore, for standard deviation, $\sigma = 0.1$ μm is chosen arbitrarily. By the usage of such μ and σ parameter values, the $g(L)$ initial normal distribution function is in the positive particle size domain, and the probability of negative diameters is negligible.

Since the evolution of the particle diameter depends only on the precipitation process, the temporal change in the i-th particle size is proportional to its growth rate

$$\frac{\partial L_i}{\partial t} \propto r_{g,i} \tag{8}$$

As a case study, the precipitation of calcium oxalate in a cuvette is investigated. The reaction can be described with equation

$$Ca^{2+} + (COO)_2^{2-} \rightarrow Ca(COO)_2 \tag{9}$$

In our model, the particles nucleate via primary nucleation. Due to the short examination times, secondary nucleation, agglomeration, and breakage are assumed to be negligible. The rate of nucleation according to the classical nucleation theory[24] can be given as

$$r_n = k_n S \exp\left(\frac{B}{\ln^2 S}\right) \tag{10}$$

where k_n is the nucleation rate coefficient and S is the supersaturation defined as

$$S = \frac{c_{Ca} c_{Ox}}{K_{sp}} \tag{11}$$

where c_{Ca} and c_{Ox} are the concentration of the reactant calcium and oxalate ions, respectively, and K_{sp} is the solubility product. The thermodynamic parameter B is defined as

$$B = \frac{16\pi\nu^2\gamma^3}{3k_B^3 T^3} \tag{12}$$

where ν is the molecular volume of the solid particle, γ is the specific interfacial energy, k_B is the Boltzmann constant, and T is the absolute temperature.

The growth of the solid particles depends not only on supersaturation but also on the surface area of the particles present in the given volume.[7] Thus, the growth rate of the solid precipitate ($r_g = \sum_i r_{g,i}$) can be expressed as

$$r_g = \frac{k_g A_p (S-1) K_{sp}}{V} \tag{13}$$

where k_g is the growth rate coefficient.

By taking into account that the particles are spherical, the amount of substance formed due to nucleation can be given as

$$n_n = \int \frac{L^3 \pi \rho_p N_p}{6M_p} g(L)\mathrm{d}L \tag{14}$$

where ρ_p and M are the density and the molar mass of the solid particle, respectively. By rearranging eq 14, the temporal change of the particle number can be given as

$$\frac{\partial N_p}{\partial t} = r_n \frac{6M_p V}{\pi\rho_p \int L^3 g(L)\mathrm{d}L} \tag{15}$$

The temporal change in the amount of substance formed due to the growth of the i-th spherical particle ($n_{g,i}$) can be expressed as

$$\frac{\partial n_{g,i}}{\partial t} = \frac{\partial}{\partial t}\left(\frac{\pi L_i^3 \rho_p}{6M_p}\right) = r_{g,i} = \frac{k_g A_{p,i} (S-1) K_{sp}}{V} \tag{16}$$

where $A_{p,i}$ is the surface of the i-th crystal, from which, after rearrangements, the temporal change in the particle volume can be given as

https://doi.org/10.1021/acsomega.3c10516
ACS Omega 2024, 9, 13412−13417

$$\frac{\partial L_i^3}{\partial t} = k_g \frac{6M_p L_i^2}{\rho_p V}(S-1)K_{sp} \tag{17}$$

Rearranging the equation and performing the derivation, we find that the temporal diameter growth of the i-th particle is independent of its own size

$$\frac{\partial L_i}{\partial t} = k_g \frac{2M_p}{\rho_p V}(S-1)K_{sp} = \frac{r_{g,i}}{A_{p,i}} \frac{2M_p}{\rho_p} \tag{18}$$

thus the growth of the particles can be given using the growth rate r_g and the total surface area of the precipitate

$$\frac{\partial L_i}{\partial t} = \frac{r_g}{A_p} \frac{2M_p}{\rho_p} \tag{19}$$

where A_p is obtained by numerical integration according to eq 3.

The second term in eq 5, which governs the crystal size dynamics, is formulated by taking the size dependence of the $f(L)$ function and applying the chain rule

$$\left.\frac{\partial f}{\partial t}\right|_{N_p} = \frac{\partial f(L_i)}{\partial t} = -\frac{\partial L_i}{\partial t}\left(\frac{\partial f}{\partial L}\right)\Bigg|_{L=L_i} \tag{20}$$

The negative sign indicates that the function $f(L)$ is shifted toward the larger particle sizes as the particles grow.

Numerical Methods. The numerical solution of eq 5 is based on an explicit Euler scheme, with the algorithm presented in Figure 1. From the initial parameters and constants, the surface area of particles (A_p) is determined in order to obtain the change in the amount of substance due to nucleation (Δn_n) and growth (Δn_g). This allows the update of reactant concentration according to

$$c_{reactant}^{t+\Delta t} = c_{reactant}^{t} - (r_n + r_g)\Delta t \tag{21}$$

where $c_{reactant}^{t}$ stands for the concentration of calcium ion and oxalate ion. The changes in particle number and size according to eqs 15 and 19 are then obtained. The $\partial f(L)/\partial L$ term is calculated, followed by an evaluation of the updated PSD function. The procedure is iterated until the end time (t_{end}) is reached.

The PSD function is discretized on 20,000 points with a spacing of 0.005 μm. The trapezoidal rule is applied to calculate both the surface area eq 3 and the volume of the particles eq 4. The $\partial f(L)/\partial L$ term in eq 5 is approximated by the central finite difference formula with a sixth-order accuracy. The PSD function is smoothed with a three−point moving average method in every 200th iteration. The simulations with a time step of Δt = 0.001 s are performed with an in-house solver written in C coupled with OpenMPI, enabling parallel computation, thus reducing the run time significantly.

For a reference data set, the previously measured temporal turbidity evolution for $Ca(COO)_2$ precipitation is used,[15] where it was shown that the turbidity dependence on concentration follows a relationship analogous to the Lambert−Beer law at the experimental conditions. Hence, the turbidity can be converted to the amount of substance in a unit volume for the product. For calibration, the saturation turbidity values are plotted as a function of equilibrium composition (c_{eq}), as shown in Figure 2. The amount of the product at equilibrium is obtained from $K_{sp} = [Ca^{2+}]_{eq}[Ox^{2-}]_{eq}$, where $[Ca^{2+}]_{eq} = [Ca^{2+}]_0 - c_{eq}$. The slope of the calibration curve presented in Figure 2 is found to be (0.3114 ± 0.0045) m^3/mol with zero intercept.

The physical constants used in the calculations are summarized in Table 1. The same temperature is set as in the experiments, and V is equal to the volume of solution in the cuvette. The kinetic reaction rate coefficient for nucleation (k_n) and growth (k_g) and the thermodynamic parameter (B)

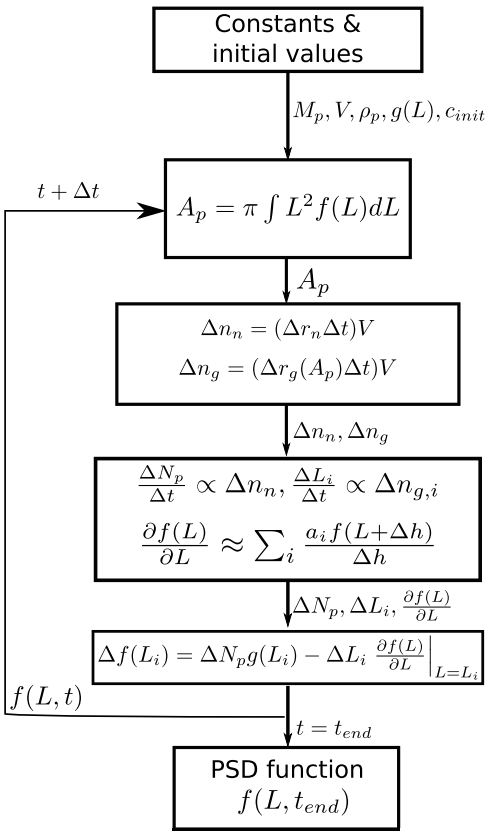

Figure 1. Algorithm of the steps applied in the numerical scheme.

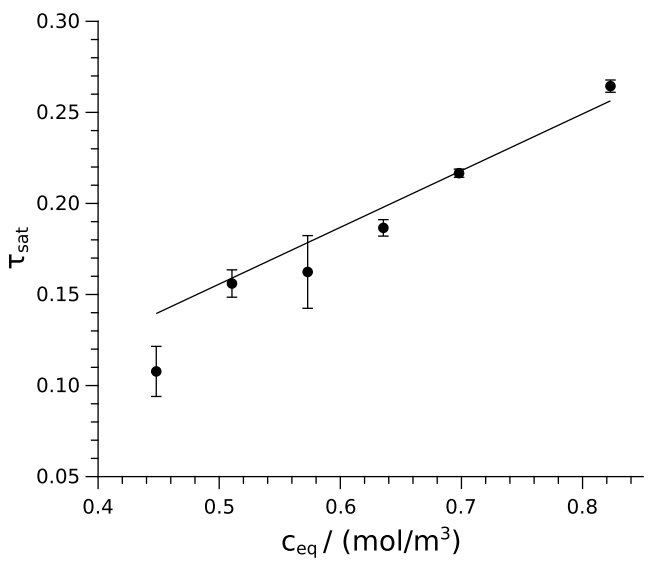

Figure 2. Calibration used to convert turbidity to the amount of product in the experimental data set.[15]

https://doi.org/10.1021/acsomega.3c10516
ACS Omega 2024, 9, 13412−13417

Table 1. Physical Quantities Used in Calculations

quantity	value	ref.
T	298 K	
V	4 cm^3	
K_{sp}	2.7×10^{-3} mol^2/m^6	25
ρ_p	2210 kg/m^3	26
M_p	128 g/mol	

are unknown; they have been determined via optimization by using Monte Carlo and simplex methods with the relative tolerance of 10^{-3}.

The Monte Carlo simulations have been executed on 10,000 parameter sets chosen randomly on the domain shown in Table 2. The goodness-of-fit is quantified with reduced chi-squared statistics

$$\chi^2 = \frac{1}{n}\sum_j \frac{(c_{e,j} - c_{c,j})^2}{\sigma_j^2} \quad (22)$$

from the corresponding measured ($c_{e,j}$) and calculated ($c_{c,j}$) values, where σ_j is the deviation of the experimental concentration at the jth sample point, and n is the degree of freedom. The experimental measurements are accessible up to 300 s; therefore, the numerical simulations are performed up to the same time range for each initial concentration. The six experimental data sets are sampled at every 0.5 s starting from 0, therefore overall m = 3606 points are used for the fitting, providing n = 3603 for the degree of freedom. The best results of the Monte Carlo simulation are then further optimized with a simplex algorithm.

Table 2. Parameter Domains Used for Monte Carlo Simulations

quantity	domain
$\log_{10}(k_n/[\text{m}^3\ \text{mol}^{-1}\ \text{s}^{-1}])$	(−10)−(+10)
$\log_{10}(k_g/[\text{m}^4\ \text{mol}^{-1}\ \text{s}^{-1}])$	(−10)−(+10)
B	(50)−(300)

RESULTS AND DISCUSSION

The optimized parameter set with a minimum of χ^2 = 15.24 has the rate coefficient of $k_n = (6.0 \pm 1.0) \times 10^{-5}$ m^3 mol^{-1} s^{-1}, the rate coefficient of $k_g = (3.7 \pm 1.0) \times 10^{-3}$ m^4 mol^{-1} s^{-1}, and the thermodynamic parameter of $B = 158.5 \pm 0.1$. Using these constants, the calculated concentration evolutions are compared to the experimental runs in Figure 3. In order to provide a physical representation of the goodness-of-fit, the average concentration deviation $\overline{\delta c}$ is determined with the formula of

$$\overline{\delta c} = \frac{1}{m}\sum_j |c_{e,j} - c_{c,j}| \quad (23)$$

Using the calibration curve obtained from Figure 2, it is then converted to average turbidity deviation $\overline{\delta\tau} = 0.0077$, which is within the experimental precision of turbidity measurements. To have a deeper insight into what influences the goodness-of-fit, we have calculated $\overline{\delta\tau}$ separately for each concentration. They fall in the range of $(2.2-13.3) \times 10^{-3}$ with the largest uncertainties associated with the measurements of c_{init} = 562.5 μm (light green symbols in Figure 3) and 875 μm (black symbols in Figure 3). In the former, the greater deviation may originate from the experimental errors, while in the latter, it originates from the conversion of turbidity values to concentrations by using the calibration curve (Figure 2), which overestimates the equilibrium concentration at high initial concentrations.

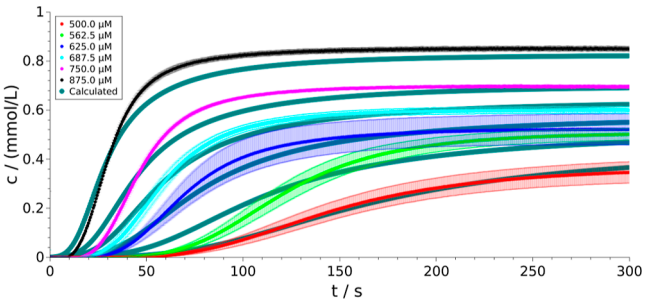

Figure 3. Temporal change of measured (colored symbols) and calculated (green solid lines) product concentrations at various initial reactant concentrations.

The calculations return the main characteristics of the temporal evolution of the formed product (Figure 3) regardless of the initial concentration: they always show an early stage, where the amount of precipitate barely increases, followed by a rapid rise that later leads to saturation. The induction time (t_{ind}) is a measure of the transition between the two regimes. It is a function of supersaturation according to

$$t_{ind} = a_S S^{-n_s} \quad (24)$$

where a_S and n_S are phenomenological parameters.[24] For the simulation, the induction time is obtained from the intercept of the straight lines fitted to the calculated data points in the first and second regimes. There is a small difference in the estimated induction times: 21% in the exponent (n_S) and 4% in the parameter a_S of eq 24, as shown in Table 3. The deviation may arise from the experimental method of acquiring induction times, since the intercept of the two fitted lines falls in a region where the turbidity is small; therefore, the deviation of the data is high.

Table 3. Experimental and Calculated Parameters of the Phenomenological Eq 24

parameter	experiment	calculation
a_S	6.31 ± 0.48	6.03 ± 0.24
n_S	2.91 ± 0.20	3.51 ± 0.06

The temporal evolution of the PSD function is presented in Figure 4. At the beginning of the precipitation process, the bell shape is sustained (Figure 4a), therefore in the initial few seconds, nucleation is dominant, corresponding to the initial part with a small slope for the selected case of c_{init} = 500 μm in Figure 3. It is followed by a regime where the PSD function starts to widen and the nucleation and growth processes become comparable. Beyond that, particle growth dominates: small particles no longer nucleate; only the existing ones grow. Thus, a shoulder will form on the left side of the $f(L)$ curve, which is associated with the greatest slope in Figure 3. From t = 200 s, the distribution curve barely changes because the saturation region is reached, in which the reactants are depleted.

https://doi.org/10.1021/acsomega.3c10516
ACS Omega 2024, 9, 13412−13417

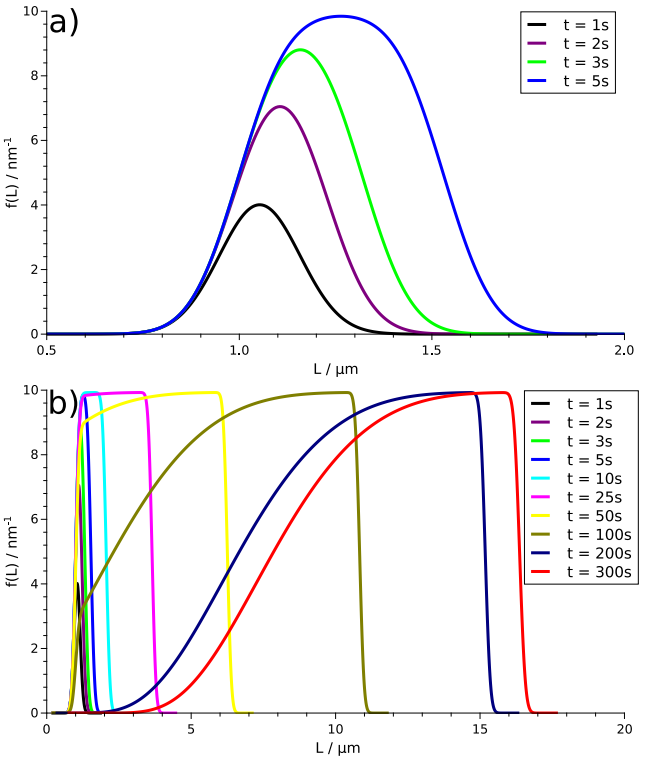

Figure 4. Evolution of PSD for c_{init} = 500 μm (a) in the first few seconds and (b) during the entire precipitation process.

The final PSD depends on the initial concentrations, according to Figure 5. At higher initial concentrations, the

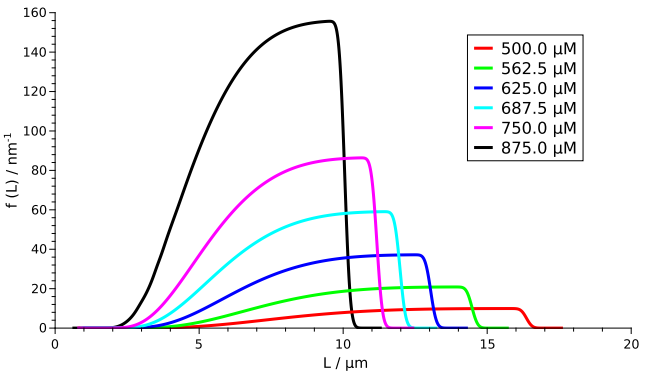

Figure 5. PSD at t = 300 s with different initial concentrations.

number of particles is larger, as indicated by the greater area under $f(L)$, however, they tend to be smaller in size. With decreasing supersaturation, the distribution curve flattens and widens toward the larger diameter sizes with decreasing area under $f(L)$, i.e., resulting in fewer but bigger particles. This is in agreement with the experiments: at high supersaturation, nucleation is dominant, while at low, particle growth is dominant.

From the SEM image reported,[15] the smallest and largest particles are measured with ImageJ software and their diameters are determined to be D = 1.84 μm and D = 8.25 μm. There is not sufficient data to create a statistical comparison, but it is adequate to conclude that the predicted PSD is in the same order of magnitude as in the experiments.

As an additional result of the fitting, the thermodynamic parameter B is also determined, from which the specific interfacial energy γ of calcium oxalate monohydrate crystals is calculated by substituting the constants in Table 1 into eq 12, yielding γ_{calc} = 38.4 mJ/m^2. The experimentally determined specific interfacial energy for calcium oxalate monohydrate is γ_{exp} = 32.4 mJ/m^2.[27] The good agreement validates our method to provide predictions for the specific interfacial energy, as well.

CONCLUSIONS

A model has been developed for precipitation processes to predict the dynamics of PSD by using product concentration time dependencies. Due to the high number of particles, population mass balance theory is used to describe the heterogeneous system. Unlike in many previous works utilizing a DPB model, experimentally measured temporal product concentration curves are used for parameter optimization instead of experimental PSDs. With this method, the evolution and the final size distributions of precipitate particles can be obtained; moreover, the specific interfacial energy can be estimated.

We have shown that the calculated concentration evolutions match the experimental curves within the range of the experimental errors. The temporal dynamics of PSDs at various initial concentrations reveals that with decreasing supersaturation, the distribution curves tend to flatten and shift toward the higher particle sizes. At high initial concentrations, nucleation is dominant, resulting in smaller but more particles. The bell shape of the distribution curve originating from the Gauss probability function is not sustained because the initial nucleation-governed regime is followed by a growth-dominated one, where significant particle growth accompanies nucleation. With comparable growth and nucleation rates, the distortion of the normal distribution shape occurs at the left side of the PSD but leaves the sharp cut-off at the right side of the curve.

The calculated specific interfacial energy value and particle sizes are compared to experimental ones, and they are also in good agreement. Hence, this approach is an appropriate method for precipitation reactions to predict the PSD and specific interfacial energy values from turbidity measurements.

Our model is applied to a system of high supersaturation by assuming isotropic precipitate particles. A systematic extension of our proof-of-concept study is the inclusion of particle geometry. This can be achieved by modifying the equations describing the volume and surface area of the particles. The numerical treatment can also be further extended to account for the dissolution of particles, and with size-dependent solubility, it can model Ostwald ripening.

AUTHOR INFORMATION

Corresponding Author

Dezső Horváth − *Department of Applied and Environmental Chemistry, University of Szeged, Szeged 6720, Hungary;* orcid.org/0000-0003-3852-6879; Email: horvathd@chem.u-szeged.hu

Authors

Paszkál Papp − *Department of Physical Chemistry and Materials Science, University of Szeged, Szeged 6720, Hungary;* orcid.org/0000-0003-3608-4886

https://doi.org/10.1021/acsomega.3c10516
ACS Omega 2024, 9, 13412−13417

Ágota Tóth − *Department of Physical Chemistry and Materials Science, University of Szeged, Szeged 6720, Hungary;* orcid.org/0000-0001-8254-6354

Complete contact information is available at: https://pubs.acs.org/10.1021/acsomega.3c10516

Notes

The authors declare no competing financial interest.

■ ACKNOWLEDGMENTS

The authors gratefully thank the financial support from the National Research, Development, and Innovation Office (K138844 and TKP2021-NVA-19). P.P. acknowledges the support from the New National Excellence Program of the Ministry for Culture and Innovation from the source of the National Research, Development, and Innovation Fund (ÚNKP-23-3-SZTE-492). The authors are grateful to the University of Szeged OpenAccess Fund (6839) for support.

■ REFERENCES

(1) Qamar, S.; Elsner, M. P.; Angelov, I. A.; Warnecke, G.; Seidel-Morgenstern, A. A comparative study of high resolution schemes for solving population balances in crystallization. *Comput. Chem. Eng.* **2006**, *30*, 1119−1131.

(2) Halfwerk, R.; Yntema, D.; Van Spronsen, J.; Keesman, K.; Van der Padt, A. Crystallization kinetics of lactose recovered at sub-zero temperatures: A population balance model combining mutarotation, nucleation and crystal growth. *J. Food Eng.* **2023**, *345*, 111412.

(3) Tang, H. Y.; Rigopoulos, S.; Papadakis, G. On the effect of turbulent fluctuations on precipitation: A direct numerical simulation—population balance study. *Chem. Eng. Sci.* **2023**, *270*, 118511.

(4) Randolph, A. D.; Larson, M. A. *Theory of particulate processes*; Academic Press: New York, 1986.

(5) Lakatos, B. G. Population balance modelling of crystallisation processes. *Hung. J. Ind. Chem.* **2007**, *35*, 7−17..

(6) Rakotozandriny, K.; Bourg, S.; Papp, P.; Tóth, Á.; Horváth, D.; Lucas, I. T.; Babonneau, F.; Bonhomme, C.; Abou-Hassan, A. Investigating CaOx crystal formation in the absence and presence of polyphenols under microfluidic conditions in relation with nephrolithiasis. *Cryst. Growth Des.* **2020**, *20*, 7683−7693.

(7) Papp, P.; Tóth, Á.; Horváth, D. Spatial precipitate separation enhanced by complex formation. *Chem. Eng. Sci.* **2022**, *261*, 117955.

(8) Puel, F.; Févotte, G.; Klein, J. P. Simulation and analysis of industrial crystallization processes through multidimensional population balance equations. Part 1: A resolution algorithm based on the method of classes. *Chem. Eng. Sci.* **2003**, *58*, 3715−3727.

(9) Hulburt, H. M.; Katz, S. Some problems in particle technology. *Chem. Eng. Sci.* **1964**, *19*, 555−574.

(10) Totis, N.; Nieto, C.; Kuper, A.; Vargas-Garcia, C.; Singh, A.; Waldherr, S. A population-based approach to study the effects of growth and division rates on the dynamics of cell size statistics. *IEEE Control Syst. Lett.* **2021**, *5*, 725−730.

(11) Colli, A. N.; Bisang, J. M. Current and potential distribution in two-phase (gas evolving) electrochemical reactors by the finite volume method. *J. Electrochem. Soc.* **2022**, *169*, 034524.

(12) McCoy, B. J. A population balance framework for nucleation, growth, and aggregation. *Chem. Eng. Sci.* **2002**, *57*, 2279−2285.

(13) Hounslow, M. J. A discretized population balance for continuous systems at steady state. *AIChE J.* **1990**, *36*, 106−116.

(14) Zauner, R.; Jones, A. G. On the influence of mixing on crystal precipitation processes—application of the segregated feed model. *Chem. Eng. Sci.* **2002**, *57*, 821−831.

(15) Das, N. P.; Zahorán, R.; Janovák, L.; Deák, Á.; Tóth, Á.; Horváth, D.; Schuszter, G. Kinetic characterization of precipitation reactions: Possible link between a phenomenological equation and reaction pathway. *Cryst. Growth Des.* **2020**, *20*, 7392−7398.

(16) Forgács, A.; Moldován, K.; Herman, P.; Baranyai, E.; Fábián, I.; Lente, G.; Kalmár, J. Kinetic model for hydrolytic nucleation and growth of TiO_2 nanoparticles. *J. Phys. Chem. C* **2018**, *122*, 19161−19170.

(17) Das, N. P.; Müller, B.; Tóth, Á.; Horváth, D.; Schuszter, G. Macroscale precipitation kinetics: Towards complex precipitate structure design. *Phys. Chem. Chem. Phys.* **2018**, *20*, 19768−19775.

(18) Guo, W.; Xia, W.; Cai, K.; Wu, Y.; Qiu, B.; Liang, Z.; Qu, C.; Zou, R. Kinetic-controlled formation of bimetallic metal−organic framework hybrid structures. *Small* **2017**, *13*, 1702049.

(19) Balog, E.; Varga, G.; Kukovecz, A.; Tóth, Á.; Horváth, D.; Lagzi, I.; Schuszter, G. Polymorph selection of zeolitic imidazolate frameworks via kinetic and thermodynamic control. *Cryst. Growth Des.* **2022**, *22*, 4268−4276.

(20) Knoll, P.; Steinbock, O. Particle aggregation modifies crystallization: Extending the hierarchical order of a polycrystalline material to the macroscale. *J. Phys. Chem. C* **2018**, *122*, 23554−23563.

(21) Zahorán, R.; Kukovecz, A.; Tóth, Á.; Horváth, D.; Schuszter, G. High-speed tracking of fast chemical precipitations. *Phys. Chem. Chem. Phys.* **2019**, *21*, 11345−11350.

(22) Quedeville, V.; Ouazaite, H.; Polizzi, B.; Fox, R. O.; Villedieu, P.; Fede, P.; Létisse, F.; Morchain, J. A two-dimensional population balance model for cell growth including multiple uptake systems. *Chem. Eng. Res. Des.* **2018**, *132*, 966−981.

(23) Elduayen-Echave, B.; Lizarralde, I.; Larraona, G. S.; Ayesa, E.; Grau, P. A new mass-based discretized population balance model for precipitation processes: Application to struvite precipitation. *Water Res.* **2019**, *155*, 26−41.

(24) Mullin, J. W. *Crystallization*; Butterworth-Heidemann: Oxford, 2001.

(25) Kotrlý, S.; Sucha, L. *Handbook of Chemical Equilibria in Analytical Chemistry*; Ellis Horwood Ltd.: Chichester, 1985.

(26) Deganello, S. The structure of whewellite, $CaC_2O_4.H_2O$, at 328 K. *Acta Crystallogr., Sect. B:. Struct. Crystallogr. Cryst. Chem.* **1981**, *37*, 826−829.

(27) Wu, W.; Nancollas, G. H. Determination of interfacial tension from crystallization and dissolution data: A comparison with other methods. *Adv. Colloid Interface Sci.* **1999**, *79*, 229−279.